Environmental Photosensitizers Can Exhibit Enhanced Actinic Absorption in Microhydrated Clusters Compared to Solution

Nabiha Hasan,*[1] Morgan Davies,*[2] Mi'Kayla Word,[3] Zifan Ma,[2] Ahren W. Jasper,[4] Joseph A. Fournier,[2†] Laura M. McCaslin[3†]

*These authors contributed equally to the manuscript
[†]Correspondence should be addressed to lmmccas@sandia.gov, jfournier@wustl.edu

Affiliations

1. Department of Chemistry, University of Southern California, Los Angeles, CA, 90089, USA.
2. Department of Chemistry, Washington University in St. Louis, St. Louis, MO 63130, USA.
3. Sandia National Laboratories, Livermore, CA 94550, USA.
4. Chemical Sciences and Engineering Division, Argonne National Laboratory, Lemont, Illinois 60439, USA.

Abstract

Brown carbon chromophores at environmental air-water interfaces often act as photosensitizers that absorb sunlight and subsequently transfer energy to nearby molecules, initiating a wide variety of chemical reactions. Despite their importance to understanding daytime chemistry at these air-water interfaces, little is known about the role of the solvation environment on the photophysical properties of these photosensitizers. In this work, we present a joint experimental-theoretical study of the vibrational and photophysical properties of microhydrated protonated and deprotonated 4-benzoylbenzoic acid (4-BBA), a key model system for environmental photosensitizers. We find that for protonated 4-BBAH$^+$·$(H_2O)_{0\text{-}1}$, representing photosensitizers in very acidic conditions, a single bright state dominates the UV-Vis spectrum between 280 and 400 nm. Comparing the experimental UV-Vis spectra and quantum chemistry-predicted spectra of 4-BBA$^+$·$(H_2O)_{0\text{-}2}$, we find that the degree of microhydration has little effect on the UV-Vis spectra or the orbitals of the dominant feature. For deprotonated 4-BBA$^-$, representing photosensitizers in basic conditions, quantum chemistry calculations predict that the UV-Vis spectra are ~3x weaker in intensity than the brightest 4-BBAH$^+$·$(H_2O)_{0\text{-}1}$ features and were not observed experimentally. Quantum chemistry calculations predict one dominant UV-Vis feature is present in the spectra of 4-BBA$^-$·$(H_2O)_{0\text{-}2}$, which exhibit minor shifts with degree of microhydration. While 4-BBA in bulk solution over a range of pH values has relatively weak absorption within the solar actinic region, we show that microhydrated 4-BBA has bright transitions within the actinic region. This indicates that the complex structure of environmental air-water interfaces can shift the absorption maximum of photosensitizers into the actinic region for enhanced absorption of sunlight and subsequent enhancement of photosensitizer-driven reactions.

1. Introduction

Environmental air-water interfaces (e.g. surfaces of the sea and sea spray aerosols) host a variety of characteristic photochemical interactions and reactions due to their unique structural and chemical properties. The photochemistry at sea spray aerosol interfaces is particularly important for developing next-generation atmospheric chemistry and climate models, as aerosol effects are currently the largest source of uncertainty in these models.[1-4] Environmental air-water interfaces are often covered with organic surfactants that may include light-absorbing compounds such as brown carbon (BrC) species.[1, 5, 6] BrC, often derived from pollutants from fossil fuel combustion, is a class of aromatic organic compounds that absorb strongly in the solar actinic region (>290 nm) and efficiently form long-lived reactive triplet species.[6] Many BrC compounds can act as photosensitizers, which are compounds that absorb sunlight to become electronically excited and subsequently transfer energy to nearby molecules, inducing chemical processes such as electron transfer and hydrogen abstraction.[7-13] These photosensitizing processes can start radical chain reactions, including production of volatile organic compounds (VOCs) and secondary organic aerosols (SOAs).[7-13]

Of recent interest are photosensitized reactions involving organic surfactant species like fatty acids at marine and sea spray aerosol interfaces to form highly functionalized VOCs via radical chain reactions.[9, 13-15] Importantly, BrC photosensitizers are competitive oxidants to $OH^{\bullet}$ and singlet oxygen. Given that the impact of aerosols remains the largest source of uncertainty in atmospheric chemistry and climate models,[1-4] it is imperative to develop a molecular-level understanding of photosensitized reaction dynamics and mechanisms at air-water interfaces. The photosensitizer species 4-benzoylbenzoic acid (4-BBA, Fig. 1) has emerged as a leading BrC model system, as it is a common moiety in chromophoric dissolved organic matter (CDOM).[9, 13, 16-21] Numerous studies have reported the kinetics and product analyses of 4-BBA reacting with common environmental organic species.[9, 13, 17-20] While the majority of studies have investigated the photophysical properties and reactions of neutral 4-BBA, recent work from Karimova et al. has shown that the photophysical properties and excited state character of 4-BBA vary significantly with protonation/deprotonation driven by varying pH.[21] 4-BBA is expected to be in the deprotonated anionic form when found in the sea surface microlayer (pH ~8; 4-BBA pK_a ~3.4). Atmospheric aerosols, on the other hand, tend to be acidic (pH ~2) and may lead to protonated forms of 4-BBA at the air-water interface.[21-24]

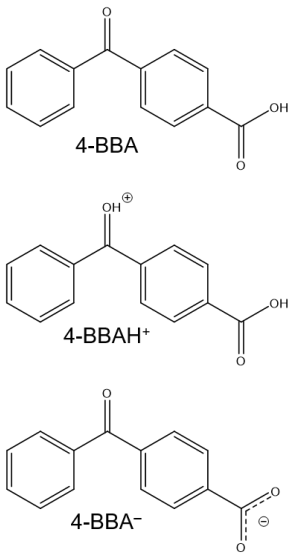

Fig. 1. Structures of neutral 4-BBA, protonated 4-$BBAH^{+}$, and deprotonated 4-BBA^{-}.

There are numerous challenges involved in unraveling detailed mechanisms of photosensitization by BrC species at air-water interfaces. Mechanistic studies of BrC photosensitizing generally rely on a combination of numerous analytical experimental techniques in concert with quantum chemistry calculations.[9, 13, 17-20] Static and time-resolved spectroscopic methods have been used to probe changes in electronic state and chemical

composition during photosensitizing processes.[9, 13, 17-20] Reaction intermediates and products are often measured via mass spectrometry techniques.[9, 13, 18] Quantum chemistry calculations such as density functional theory (DFT) are commonly performed to aid assignment of spectra, reveal reaction energetics, and confirm mechanisms.[13, 20, 21] Experimental probes of the complex structure and makeup of environmental air-water interfaces, including interface-sensitive spectroscopic methods, are challenging to interpret due to their broad features and the difficulty of predicting spectra theoretically.[25, 26] Furthermore, air-water interfaces have unique properties that change how molecules behave; in particular, acid-base chemistry has been shown to differ substantially between air-water interfaces and in bulk.[23, 24, 27-29] Experimental and theoretical studies of clusters have emerged as one of the leading models for investigating the unique chemistry that occurs at air-water interfaces.[23, 30-33]

Despite the many insights obtained from quantum chemistry calculations in concert with spectroscopic experiments, complex and dynamical interfacial environments pose a significant challenge for constructing a small molecular cluster system that represents the key chemistry of a photosensitizing reaction. Experimental techniques based on action spectroscopy of size-selected clusters have long been viewed as a precise way to investigate of the dependence of electronic and vibrational structure as a function of cluster size.[34-37] In these experiments, properties such as system composition, charge state, and degree of hydration are known and precisely controlled. To our knowledge, such experiments investigating the degree of hydration and charge state on the vibrational and electronic structure of size-selected microhydrated photosensitizer clusters have not been published. Herein we report a joint experimental-theoretical study of the vibrational and electronic structure of protonated 4-BBA$H^+\cdot(H_2O)_{0\text{-}2}$ and deprotonated 4-BB$A^-\cdot(H_2O)_{0\text{-}2}$. We investigate the changes to the vibrational and electronic spectra with respect to molecular structure, degree of microhydration, and protonation state via action spectroscopy and quantum chemical calculations.

2. Methods

2.1. Experimental Methods

The WashU cryogenic ion photofragmentation mass spectrometer has been described in detail elsewhere.[38] Briefly, ions were generated through electrospray ionization of 1 mM solutions of 4-BBA (Sigma-Aldrich, used without further purification) in 3:1 v:v acetonitrile:methanol. Trace formic acid was added to the solution for formation of the protonated cation, while trace NaOH was used to form the deprotonated anion. The ions were guided through three differentially pumped stages uses RF-only hexapole ion guides into a three-dimensional quadrupole Paul trap (Jordan TOF, Inc.) attached to a closed-cycle helium cryostat (Janis Research). Helium buffer gas was introduced into the ion trap through a pulse valve (Parker Hannifin, Series 9 general valve) and the ions were collisionally cooled to either 28 K or 170 K. Formation of "tagged" complexes between parent ions and N_2 (28 K) or water (170 K) within the trap were facilitated by trace nitrogen and water in the buffer gas. A low amplitude RF pulse on resonance with the secular frequency of the untagged parent ion was applied to the trap entrance electrode to remove these ions from the trap. After sweeping, laser pulses were loosely focused into the trap through a KBr window using a spherical mirror. All ions remaining after the laser interactions were extracted into

a reflectron time-of-flight (TOF) mass spectrometer (Jordan TOF, Inc.). Ion signal was detected with a dual-channel microchannel plate (MCP) detector.

IR action spectra were recorded using a tunable IR optical parametric oscillator/amplifier (OPO/OPA) system (LaserVision). The OPO/OPA system was pumped by a Nd:YAG laser (Continuum Surelite EX, 10 Hz, 7 ns pulse duration, 660 mJ per pulse) and the output was tunable across the 2000-4500 cm^{-1} range, with pulse energies varying between 2 and 40 mJ per pulse. The lower-frequency range (800-2200 cm^{-1}, 0.1-1 mJ per pulse) was generated by difference frequency mixing of the OPA signal and idler beams in an $AgGaSe_2$ crystal. The resolution of the system is ~3 cm^{-1}. Action spectra were collected by recording the N_2 or H_2O photodissociation yield as a function of the IR frequency. The reported spectra are averages of 10-20 scans, with data binned at 1 cm^{-1} interval. The spectra were normalized by dividing by the laser power at each frequency to account for variation in the laser power over the scanning range.

UV-Vis action spectra were recorded using the output of a tunable OPA (Light Conversion, TOPAS Prime) pumped by a Ti:Sapphire oscillator/regenerative amplifier laser system (Coherent Astrella, 800 nm, 1 kHz, 35 fs, 3.6 W). The output bandwidth of the UV-Vis pulses is ~5 nm across the tuning range used in these studies (285-490 nm). The pulse energies were kept at ~3 μJ/pulse at each wavelength using a half-waveplate and polarizer. Action spectra were collected by recording the photofragmentation yield at intervals of 5-10 nm. The photofragmentation signal was averaged over 128 trapping cycles, with 10 total averages collected at each wavelength.

2.2. Computational Methods

A conformer search for each of the six clusters was performed in Crest,[39] where all structures with a relative energy within 1 eV of the lowest-lying cluster were selected for secondary screening. These lowest-lying clusters underwent geometry optimization with the B3LYP density functional,[40-43] STO-6G basis set,[44] and D3(BJ) dispersion correction.[45] The 10 lowest-lying structures from each cluster in this secondary screening were then optimized a second time with the same density functional and dispersion correction and the aug-cc-pVDZ basis set.[46, 47] Harmonic frequency calculations were performed at the B3LYP-D3(BJ)/aug-cc-pVDZ level of theory to confirm that all structures are geometric minima, obtain zero-point energies (ZPE), and obtain vibrational frequencies. Zero-point energy (ZPE) was included in calculations of the relative energy to identify the lowest-lying conformer. Vibrational frequencies of 4-$BBAH^+\cdot(H_2O)_n$ were scaled by 0.956 to bring the carboxylic acid OH stretch of 4-$BBAH^+$ into agreement with experiment. Vibrational frequencies of 4-$BBA^-\cdot(H_2O)_n$ were scaled by 0.962 to bring the strongest calculated CH stretch of 4-BBA^- into agreement with the strongest measured CH stretch. To obtain the UV-Vis spectra, vertical excited state calculations were performed at the minimum geometries for the lowest-lying isomers of each cluster with time-dependent density functional theory (TDDFT), employing the same functional, basis set, and dispersion correction as used in the ground state calculations. UV-Vis energies of 4-$BBAH^+\cdot(H_2O)_n$ were all scaled 0.925 to bring the most intense feature of 4-$BBAH^+$ into agreement with experiment. Natural transition orbitals (NTOs) were computed and visualized in IQMol[48] with an isovalue of 0.02 $Å^{-3}$ to represent the changes in electronic density during an electronic transition.

3. Results and Discussion

3.1. Protonated 4-BBA Cation

3.1.1. Structures and Infrared Spectra

Vibrational action spectra of 4-BBAH$^+$·N_2 and 4-BBAH$^+$·H_2O are presented in Figs. 2a and 2b, respectively, along with the calculated harmonic spectra for the minimum-energy structures (shown inset). For the bare 4-BBAH$^+$ species, the excess proton can bind to either the bridging ketone carbonyl or the carboxylic acid carbonyl. Our calculations predict the protonated ketone species to be 4731 cm^{-1} lower in energy compared to protonation at the carboxylic acid group. Protonation of the ketone group gives rise to two intense OH stretch infrared (IR) transitions from the protonated OH$^+$ ketone group and from the OH stretch of the carboxylic acid group. The calculations predict these two OH stretch transitions to be nearly isoenergetic. The experimental vibrational spectrum also displays two strong high-frequency transitions, but with a larger separation than predicted. The lower-energy feature occurs at 3403 cm^{-1} and is broader (Full-width half maximum (FWHM) 21 cm^{-1}) than the higher-energy transition at 3573 cm^{-1} (FWHM 9 cm^{-1}). We assign the 3403 cm^{-1} transition to the OH$^+$ stretch from the ketone group, red shifted and broadened due to a relatively strong interaction with the N_2 tag molecule which preferentially binds to the charge center. The 3573 cm^{-1} transition is, therefore, assigned to the carboxylic acid OH stretch. Calculations with a bound N_2 molecule accurately capture the observed experimental splitting between the ketone and carboxylic acid OH stretches (Fig. S1). Furthermore, the experimental fingerprint region (1000-1900 cm^{-1}) is more consistent with the predicted spectrum for protonation at the ketone group compared to at the carboxylic acid group (Fig. S2).

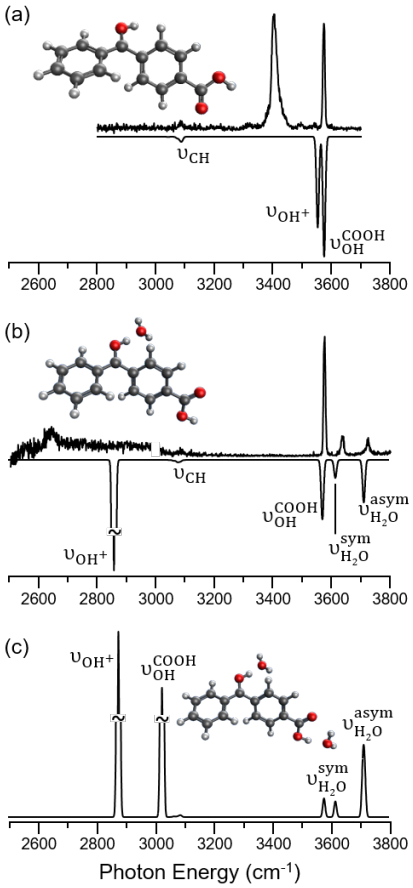

Fig. 2. Vibrational action spectra and harmonic calculations for the minimum-energy structures of 4-BBAH$^+$·$(H_2O)_{0-2}$ complexes. (a) Bare 4-BBAH$^+$ tagged with a single N_2 molecule. (b) 4-BBAH$^+$·H_2O. (c) Calculated 4-BBAH$^+$·$(H_2O)_2$ IR spectrum. All calculations were scaled by 0.956 to bring the carboxylic acid OH stretch of bare 4-BBAH$^+$ into agreement with experiment. Each calculated transition was Gaussian broadened with a FWHM of 10 cm^{-1}.

In the one-water cluster, the water molecule can bind either at the protonated ketone site or at the carboxylic acid group via H-bonding interactions. The experimental spectrum (Fig. 2b) exhibits a transition at 3573 cm^{-1}, which is the same frequency assigned to the carboxylic acid OH stretch in the bare cation. In the one-water cluster, there is no feature corresponding to a protonated ketone OH$^+$ stretch at 3403 cm^{-1}, as seen in the bare cation. The lack of the ketone

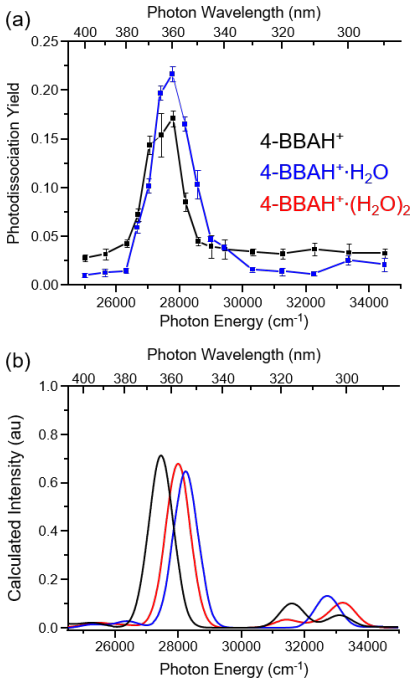

Fig. 3. (a) UV-Vis action spectra of 4-BBAH$^+$ (black) and 4-BBAH$^+$·H_2O (blue), each showing a single main transition near 27500 cm^{-1} (364 nm). (b) Calculated UV spectra for 4-BBAH$^+$ (black), 4-BBAH$^+$·H_2O (blue) and 4-BBAH$^+$·$(H_2O)_2$ (red). Each spectrum was scaled by 0.925 and Gaussian broadened with a FWHM of 1000 cm^{-1}.

OH$^+$ stretch is consistent with the water binding to the OH$^+$ ketone group. Additionally, two new transitions appear at 3633 cm^{-1} and 3720 cm^{-1}, which we assign as the symmetric and antisymmetric stretches of the bound water, respectively. The appearance of a symmetric and antisymmetric OH stretch normal mode pair indicates that the water molecule accepts a single H-bond from the ketone OH$^+$ group and donates no H-bonds. In this arrangement, the ketone OH$^+$ stretch would be expected to show a significant red shift due to formation of a strong ionic H-bond with the water molecule.[49, 50] Indeed, a highly red shifted and broad feature (2500-3200 cm^{-1}) is observed with highest intensity near 2640 cm^{-1}, consistent with strong and highly anharmonic H-bonded OH stretch transitions.[49, 50] Note that this lower-frequency region was collected at full laser power and likely results from multiphoton absorption due to the large binding energy (~3000 cm^{-1}) of water molecules. The spectral assignments are corroborated by the calculations, as the ketone-bound water arrangement is predicted to be the lowest-energy isomer. The calculated harmonic spectra are also in good agreement with the experimental spectra.

The calculated minimum-energy structure and harmonic IR spectrum of 4-BBAH$^+$·$(H_2O)_2$ are presented in Fig. 2c for further comparison. Sufficient ion signal of this species could not be generated for spectroscopic characterization. Our theoretical calculations find that the second water molecule binds to the carboxylic acid OH group, accepting a single H-bond. One OH group of the water molecule points towards the carboxylic acid carbonyl, but the H-bond interaction is weak, evidenced by a small angle of 118° between OH and carbonyl. This weak interaction enables the symmetric and antisymmetric stretch character of the bound water molecule to be retained. The calculations predict a small difference between the two respective symmetric stretches (41 cm^{-1}, unscaled) and nearly isoenergetic antisymmetric stretches (6 cm^{-1}, unscaled). Based on our observations of the single-water cluster, we predict that if ion signal were sufficiently strong to measure the two-water cluster, we predict that the H-bonded carboxylic acid OH stretch group would significantly red shift and broaden like the H-bonded ketone OH$^+$ group in the single water complex. This prediction is supported by the theoretical calculations showing that the carboxylic acid OH stretch in the two-water cluster is 574 cm^{-1} red shifted (unscaled) from the one-water cluster.

There are several low-lying conformers (< 300 cm^{-1} difference in relative energy) for each of the protonated cation species that involve internal rotations of the 4-BBAH$^+$ COH$^+$ and COOH groups. The IR and electronic spectra of these conformers are essentially identical to those for the minimum-energy structures and are likely to be indistinguishable experimentally (Figs. S3-S11).

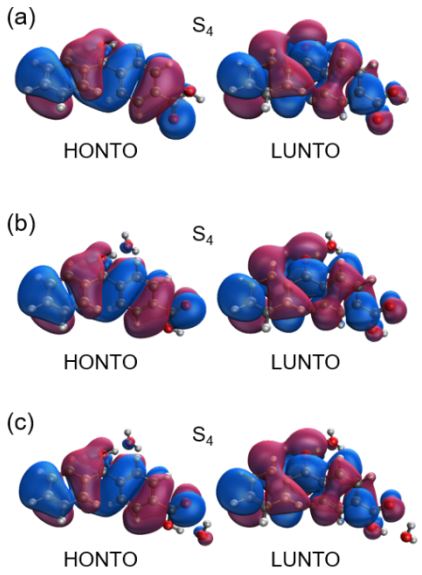

Fig. 4. NTOs corresponding to the most intense UV-Vis transitions (S_4 state) predicted in Fig. 3b. (a) 4-BBAH$^+$. (b) 4-BBAH$^+$·H_2O. (c) 4-BBAH$^+$·$(H_2O)_2$. The calculations predict a ππ* transition for each species.

3.1.2. UV-Vis Spectra and Electronic Transitions

Low-resolution UV-Vis spectra of 4-BBAH$^+$ and 4-BBAH$^+$·H_2O are presented in Fig. 3a, with calculated spectra given in Fig. 3b. A single strong transition is observed in both species. As stated above, sufficient ion signal of 4-BBAH$^+$·$(H_2O)_2$ could not be generated for spectroscopic characterization. The UV-Vis spectra of 4-BBAH$^+$ were measured with two photofragmentation methods: photofragmentation of the bare 4-BBAH$^+$ as well as photofragmentation of 4-BBAH$^+$ tagged with N_2. The UV-Vis spectrum collected from the bare 4-BBAH$^+$ photofragmentation gives a maximum absorption center at ~27500 cm^{-1} (~364 nm), see Fig. S12. The UV-Vis spectrum collected from the N_2-tagged 4-BBAH$^+$ exhibits a small blue shift of 300 cm^{-1} in the maximum peak (27800 cm^{-1}, ~360 nm) compared to the bare, see Fig. S13. The UV-Vis spectrum of 4-BBAH$^+$·H_2O was collected by monitoring the loss of the H_2O, showing an absorption maximum at (27800 cm^{-1}, ~360 nm). Interestingly, this shows that the absorption maximum in the UV-Vis spectrum of the N_2-tagged 4-BBAH$^+$ is very close to that of the 4-BBAH$^+$·H_2O, indicating a similar solvatochromic shift from loss of N_2 vs. H_2O.

The calculated UV-Vis spectra in Fig. 3b are in good agreement with experiment, as they correctly predict one intense transition for both 4-BBAH$^+$ and 4-BBAH$^+$·H_2O. Furthermore, the calculations predict a 793 cm^{-1} blue shift (unscaled) between the absorption maxima of 4-BBAH$^+$ and 4-BBAH$^+$·H_2O, compared to a blue shift of ~300 cm^{-1} in the experiment. The calculated UV-Vis spectrum of the 4-BBAH$^+$·$(H_2O)_2$ minimum-energy structure is also presented in Fig. 3b. The calculated spectrum is quite similar to both 4-BBAH$^+$ and 4-BBAH$^+$·H_2O, with the absorption maximum predicted to fall in-between those of 4-BBAH$^+$ and 4-BBAH$^+$·H_2O. Natural transition orbitals (NTOs) of each species' most intense UV-Vis transition, the S_4 state, are shown in Fig. 4. The highest occupied NTO (HONTO) and lowest unoccupied NTO (LUNTO) represent the initial and final orbitals in the electronic transition. The HONTOs for each species look very similar, as well as the LUNTOs, indicating that the complexation of 1-2 water molecules plays only a minor role in the electronic structure of the bright state S_4. The NTOs indicate that the S_4 states are primarily characterized by a ππ* transition. In the water-complexed clusters, some electron density can be seen on the water molecules bound to the protonated ketone, though the majority of electron density is on the 4-BBAH$^+$ species.

Each of the 4-BBAH$^+$·$(H_2O)_n$ species are predicted to have weaker higher-energy transitions that fall within the 31000-34000 cm^{-1} (294-323 nm) range. Although absorption signal may be present in this region experimentally, the signals are too weak to distinguish above the baseline noise. Our theoretical calculations reveal that the NTOs for these higher-energy transitions correspond primarily to ππ* transitions (Fig. S14).

Overall, the UV-Vis spectra of microhydrated 4-BBAH$^+$ display absorption maxima in the 350-375 nm range, which is quite shifted compared to 4-BBA in bulk water at low pH (~260 nm).[21] We note that 4-BBA in bulk water at low pH also exhibits a weak, broad shoulder at ~330 nm. For a number of reasons, it is unclear whether we can make a one-to-one comparison between the strongest features in the bulk vs. cluster spectra. Due to experimental limitations, we are unable to scan the UV-Vis region to higher energies where microsolvated 4-BBAH$^+$ may exhibit maximum absorption. We turn to theoretical calculations to assess whether intense features arise at higher excitation energies, finding that within the studied range, up to 235 nm, there are no stronger peaks. Furthermore, we note that, to our knowledge, the photophysical properties of microsolvated 4-BBAH$^+$ have not been studied, as 4-BBAH$^+$ may not be stable in bulk solution. The pK_a of the carboxylic acid OH in 4-BBAH$^+$ is 3.4.[21] The ketone OH$^+$ pK_a of 4-BBAH is likely much smaller, though to our knowledge, a literature value is not available. This means that 4-BBAH$^+$ will likely exist only in highly acidic, undersolvated conditions that can occur at air-water interfaces. Numerous studies have found that the unique conditions of the air-water interface can result in stabilization of intact strong acids such as HCl and HNO_3.[23, 24, 27-29]

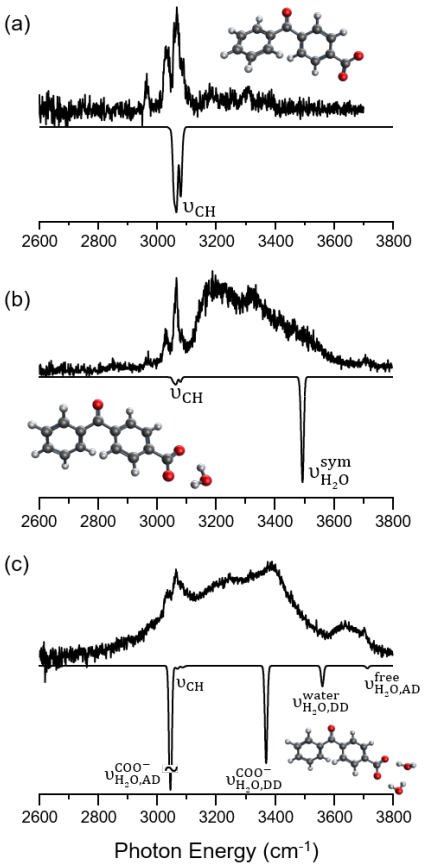

Fig. 5. Vibrational action spectra and harmonic calculations for 4-BBA$^-$·$(H_2O)_{0\text{-}2}$ complexes. (a) Bare 4-BBA$^-$ tagged with a single N_2 molecule. (b) 4-BBA$^-$·H_2O. (c) 4-BBA$^-$·$(H_2O)_2$. All calculations were scaled by 0.962 to bring the strongest calculated CH stretch into agreement with the strongest measured CH stretch in bare 4-BBA$^-$.

Interestingly, we observe minimal perturbation by one and two water molecules on the UV-Vis spectrum of bare 4-BBAH$^+$, indicating that a much larger hydration shell is needed to shift the electronic transitions closer to the bulk solution spectrum, which will likely cause the protonated ketone to deprotonate and form neutral 4-BBA and H_3O^+. Future studies investigating the photophysical properties of larger cationic 4-BBAH$^+$·$(H_2O)_n$ (n>2) clusters are needed to investigate these questions. All said, the relatively strong ππ* transitions of microhydrated 4-BBAH$^+$ fall well within the solar actinic region, suggesting that protonated 4-BBA could be a highly active photosensitizer at the surface of acidic aerosols.

3.2 Deprotonated 4-BBA Anion

3.2.1 Structures and IR Spectra

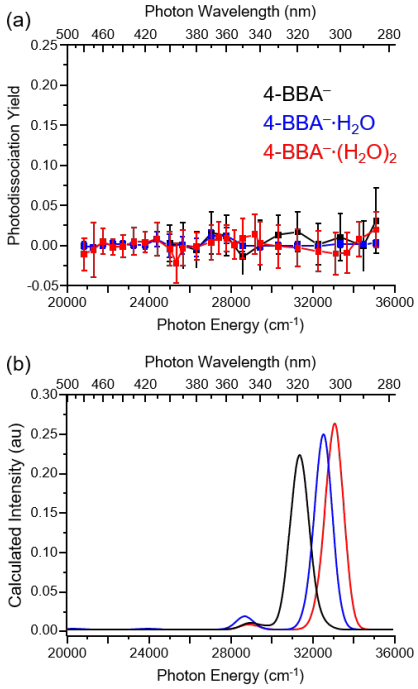

Fig. 6. (a) UV-Vis action spectra of 4-BBA$^-$ (black), 4-BBA$^-$·H_2O (blue), and 4-BBA$^-$·$(H_2O)_2$ (red). No transitions are apparent above experimental uncertainty. The intensity scale is the same as that in Fig. 3b. (b) Calculated UV-Vis spectra. The calculated transitions are unscaled and Gaussian broadened by 1000 cm^{-1}.

Vibrational action spectra of deprotonated 4-BBA$^-$·$(H_2O)_{0\text{-}2}$ clusters are presented in Fig. 5 along with scaled harmonic spectra of the minimum-energy structures. For bare 4-BBA$^-$, the vibrational spectrum in the high-frequency region only displays relatively weak CH stretching modes, as expected for a deprotonated species without strong OH oscillators (Fig. 5a). The lower-frequency fingerprint region is presented in Fig. S15 showing the ketone and carboxylate group CO stretching modes, confirming the identity of the 4-BBA$^-$ anion.

The vibrational spectrum of 4-BBA$^-$·H_2O shows a broad OH stretching region spanning 3100-3500 cm^{-1} that is consistent with the calculated minimum-energy structure where the water molecule forms two H-bonds with the carboxylate in a bridging configuration (Fig. 5b). The harmonic calculations predict an intense transition in this region deriving from the water symmetric stretch mode, $\upsilon_{H_2O}^{sym}$. The antisymmetic stretch (not pictured), $\upsilon_{H_2O}^{asym}$, is theoretically predicted to carry little oscillator strength. Overall, the breadth and substructure of the OH stretch band is consistent with strong anharmonic coupling typically seen in ionic water cluster systems.[51-53] Deviations between experiment and the harmonic approximation in this region are well understood and expected.

Turning to the vibrational spectrum of 4-BBA$^-$·$(H_2O)_2$ (Fig. 5c), the OH stretch region is even broader than the one-water complex, spanning 3000-3500 cm^{-1}. The calculated minimum-energy structure predicts that both water molecules bind to the carboxylate group. The binding of the two water molecules at the carboxylate group is consistent with the recent calculations from Karimova et al.[21] on 4-BBA$^-$ clustered with 8 and 30 water molecules which showed extended water networks forming around the carboxylate group. One water is in a double donor (DD) arrangement, donating a H-bond each to the carboxylate group and to the other water molecule. The other water molecule is in an acceptor-donor (AD) configuration, donating a H-bond to the carboxylate group and accepting a H-bond from the other water, leaving a free OH. The weaker high-frequency feature at 3650 cm^{-1} is consistent with the predicted OH stretch of the double donor water molecule towards the other water molecule, $\upsilon_{H_2O,DD}^{water}$. The sharper transition emerging from this broad feature at 3702 cm^{-1} derives from the free OH stretch of the AD water molecule, $\upsilon_{H_2O,AD}^{free}$. The remaining broad features in the 3000-3500 cm^{-1} range are consistent with the predicted OH stretch of the DD water towards the carboxylate group, $\upsilon_{H_2O,DD}^{COO^-}$. The remaining H-bonded OH stretch of the AD water, $\upsilon_{H_2O,AD}^{COO^-}$ is

likely broad, similar to $\upsilon^{COO^-}_{H_2O,DD}$, extending to frequencies in the CH stretching region. We assign the features at ~3065 cm^{-1} to CH stretches broadened by $\upsilon^{COO^-}_{H_2O,AD}$.

3.2.2 UV-Vis Spectra and Electronic Transitions

Spectral scans in the 20000-36000 cm^{-1} (280-500 nm) range for 4-BBA$^-$·(H$_2$O)$_{0\text{-}2}$ clusters are shown in Fig. 6a. No discernable transitions above baseline noise were observed for any of the three species experimentally. Electron photodetachment, which would result in depletion of the parent anion due to formation of the corresponding neutral, was not observed. Turning to the calculated UV-Vis spectra in Fig. 6b, we find that each cluster 4-BBA$^-$·(H$_2$O)$_{0\text{-}2}$ exhibits one dominant feature in the 280-500 nm range. However, we note that these features are ~3x less intense than the most intense features in the predicted 4-BBAH$^+$·(H$_2$O)$_{0\text{-}2}$ clusters. We note that we theoretically predict less intense features in the 4-BBAH$^+$·(H$_2$O)$_{0\text{-}2}$ UV-Vis spectra at ~300-320 nm (Fig. 3b) which have similar intensities as those predicted for 4-BBA$^-$·(H$_2$O)$_{0\text{-}2}$. Because these lower intensity features in 4-BBAH$^+$·(H$_2$O)$_{0\text{-}2}$ could not be observed experimentally, it is likely that the intensities of 4-BBA$^-$·(H$_2$O)$_{0\text{-}2}$ are similarly too low for experimental measurement. While there is an experimental increase in photodissociation signal near the end of the tuning range (~285 nm), it is not definitively above the noise level of the measurement. We thus rely on theoretical calculations for our analysis.

Fig. 6b shows the UV-Vis spectra of 4-BBA$^-$·(H$_2$O)$_{0\text{-}2}$ predicted theoretically. We observe that the bare 4-BBA$^-$ exhibits a strong transition at ~320 nm. Upon complexation with one water, this peak shifts to ~310 nm and with a second water molecule, shifts again to ~300 nm. In contrast to 4-BBAH$^+$·(H$_2$O)$_{0\text{-}2}$, we observe systematic blue shifting of the dominant feature. A lack of systematic shift in the 4-BBAH$^+$·(H$_2$O)$_{0\text{-}2}$ is likely due to the fact that each water binds to a different functional group site (carboxylic acid and protonated ketone), while in 4-BBA$^-$·(H$_2$O)$_{0\text{-}2}$, both the one- and two-water clusters bind to the carboxylate.

The NTOs of the dominant UV-Vis transitions of 4-BBA$^-$·(H$_2$O)$_{0\text{-}2}$ are shown in Fig. 7. These NTOs represent the electronic orbitals for the S_{17} state of the bare anion, S_{14} state of the one-water, and S_9 state of the two-water. This represents another difference between the 4-BBA$^-$·(H$_2$O)$_{0\text{-}2}$ and 4-BBAH$^+$·(H$_2$O)$_{0\text{-}2}$ UV-Vis spectra: all the intense features in the 4-BBAH$^+$·(H$_2$O)$_{0\text{-}2}$ correspond to the same electronic state, S_4. However, despite the differences in state ordering, the NTOs of 4-BBA$^-$·(H$_2$O)$_{0\text{-}2}$ show many similar characteristics. We assign these NTOs as primarily ππ* transitions. Karimova et al. found that 4-BBA$^-$·(H$_2$O)$_8$ exhibits a bright ππ* transition at ~275 nm with similar NTO orbital characteristics as we found for 4-BBA$^-$·(H$_2$O)$_2$. While cluster studies of the UV-Vis spectra of 4-BBA$^-$·(H$_2$O)$_{3\text{-}8}$ are needed to confirm this, we

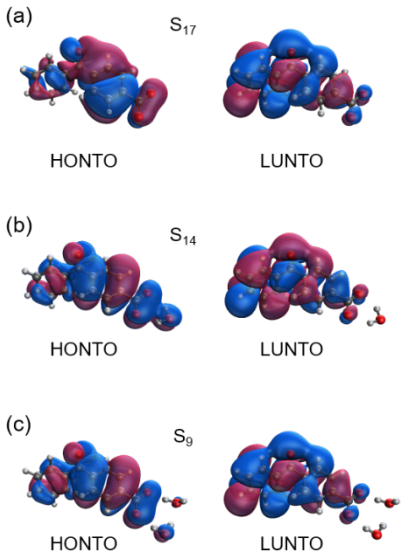

Fig. 7. NTOs corresponding to the strongest UV transitions predicted in Fig. 6b. (a) 4-BBA$^-$. (b) 4-BBA$^-$·H$_2$O. (c) 4-BBA$^-$·(H$_2$O)$_2$.

hypothesize that adding water to the solvation shell around 4-BBA$^-$·$(H_2O)_n$ systematically blue shifts the dominant ππ* feature toward the high-pH solution-phase limit of 264 nm. While the UV-Vis absorption peaks of microhydrated 4-BBA$^-$ are predicted to be fairly weak, they appear in the solar actinic region where even weakly absorbing chromophores can significantly drive photochemical reactions.[54, 55]

Finally, we assessed the role of protonation/deprotonation on the shift of the UV-Vis spectrum by comparing the calculated UV-Vis spectra of microhydrated 4-BBAH$^+$ and 4-BBA$^-$ (Figs. 3b, 6b) with the neutral 4-BBA (Fig. S16). Due to the nature of our action spectroscopy experiments, neutral species cannot be mass selected for study. We find that all three clusters (0-2 water molecules, H-bound to carboxylic acid) exhibit the dominant UV-Vis absorption feature at 256 nm (unscaled). This is close to the experimental value of 4-BBA in bulk water, with an absorption peak of 260 nm.[21] Karimova et al. found a maximum UV-Vis absorption feature of 4-BBA·$(H_2O)_8$ at 265 nm with similar computational methods as the ones used here.[21] Thus, our value of 256 nm in 4-BBA·$(H_2O)_{0\text{-}2}$ is blue shifted relative to the larger clusters and experimental values of 4-BBA in bulk solution. This indicates that the trend seen for microhydrated 4-BBA$^-$, where the addition of water blue shifts the dominant UV-Vis peak away from the actinic region, is not observed for systematic hydration of neutral 4-BBA. We also note that the dominant UV-Vis peaks of 4-BBA·$(H_2O)_{0\text{-}2}$ is blue shifted relative to those observed in 4-BBA$^-$·$(H_2O)_{0\text{-}2}$ as well as 4-BBAH$^+$·$(H_2O)_{0\text{-}2}$ This indicates that protonation/deprotonation of 4-BBA can result in shifting the dominant UV-Vis features into the actinic region in addition to reduction in degree of hydration. Further study into the role of solvation environment, including charge state, degree of microhydration, pH, and molecular configuration is needed to achieve a molecular-level mechanistic picture of photosensitizing reactions at air-water interfaces.

4. Conclusion

Air-water interfaces in the environment, including the sea surface microlayer and sea spray aerosols, are unique environments for molecular reactions, driving chemistry with fundamentally different mechanisms than in the gas phase or in bulk water. One particularly important and challenging class of processes are driven by BrC photosensitizers, which absorb sunlight and transfer energy to nearby molecules.[7-13] These photosensitizer-initiated reactions can incite processes such as electron transfer, often resulting in a cascade of radical reactions, dynamically affecting the structure and composition of environmental air-water interfaces. Detailed mechanisms of photosensitizing processes are extremely difficult to unravel at a molecular level due to the complexity of air-water interface structures, resulting in broad spectroscopic features. Spectroscopic studies of size-selected clusters have long been used to model chemistry at air-water interfaces for precise investigation of how cluster size and conformer affect the vibrational and electronic structure of molecular processes.[23, 30-33]

In this work we investigate the role of charge state and microhydration on the electronic and vibrational spectroscopy of the deprotonated and protonated forms of 4-BBA clustered with 0-2 water molecules. Size-selected clusters of 4-BBAH$^+$·$(H_2O)_{0\text{-}1}$ and 4-BBA$^-$·$(H_2O)_{0\text{-}2}$ were generated and studied with UV-Vis and IR action spectroscopy alongside quantum chemistry calculations; ion signals of 4-BBAH$^+$·$(H_2O)_2$ were too low for experimental observation, though quantum chemistry calculations were performed to predict their spectra and electronic structure. Vibrational action spectroscopy was used in concert with conformer searches to assign the lowest-

lying minimum structures for each cluster. UV-Vis action spectroscopy on the size-selected clusters was performed to determine how absorption peaks of protonated and deprotonated 4-BBA complexes shift with degree of microhydration. With the support of quantum chemistry calculations, we find that 4-BBAH$^+$·$(H_2O)_{0\text{-}2}$ exhibits one dominant feature in the 280-500 nm range that shifts non-systematically with addition of water molecules. We hypothesize that this is due to there being two binding sites for H_2O, one at the carboxylic acid and one at the protonated ketone. Shifts in the UV-Vis absorption maximum 4-BBAH$^+$ are thus significantly dependent on the specific configuration and solvation environment. While the UV-Vis features of 4-BBA$^-$·$(H_2O)_{0\text{-}2}$ were not strong enough to observe experimentally, quantum chemistry calculations predict that each cluster exhibits one strong absorption feature that shifts systematically to the blue as water molecules are added. This systematic blue shift occurs because water binds preferentially to the carboxylate, even up to 8 water molecules.[21] Our experimental measurements find that 4-BBAH$^+$·$(H_2O)_{0\text{-}1}$ absorbs in the solar actinic range and quantum chemistry calculations find that this is also true of 4-BBAH$^+$·$(H_2O)_2$. Quantum chemistry calculations predict that 4-BBA$^-$·$(H_2O)_{0\text{-}2}$ UV-Vis absorption features are about a factor of 3x less intense than the dominant transitions in 4-BBAH$^+$·$(H_2O)_{0\text{-}2}$. Interestingly, the undersolvated clusters we studied should all exhibit absorption in the solar actinic range, which is not true of 4-BBA and 4-BBA$^-$ in bulk water. This indicates that the unique microhydration conditions of air-water interfaces can enhance the photosensitizing activity of BrC compounds and their subsequent reaction cascades.

CRediT authorship contribution statement

Nabiha Hasan: Investigation, formal analysis, data curation, writing – review and editing. **Morgan Davies:** Investigation, formal analysis, data curation, writing – review and editing. **Mi'Kayla Word:** Investigation, writing – review and editing. **Zifan Ma**: Investigation, writing – review and editing. **Ahren W. Jasper:** Conceptualization, methodology, writing – review and editing. **Joseph A. Fournier:** Conceptualization, data curation, formal analysis, methodology, project administration, supervision, validation, visualization, writing – original draft. **Laura M. McCaslin:** Conceptualization, data curation, formal analysis, funding acquisition, investigation, methodology, project administration, supervision, validation, writing – original draft.

Declaration of competing interests

There are no conflicts of interests.

Data Availability

The data supporting the findings will be uploaded to the publicly accessible database Figshare upon acceptance.

Acknowledgments

N.H. acknowledges that this work was supported in part by the U.S. Department of Energy (USDOE), Office of Science, Office of Workforce Development for Teachers and Scientists (WDTS) under the Science Undergraduate Laboratory Internships (SULI) program. N.H. also acknowledges support from the USDOE Scholars Program. M. Word and L.M.M are grateful for funding from the Division of Chemical Sciences, Geosciences and Biosciences, Office of Basic Energy Sciences (BES), USDOE, which supported the scientific research, including acquisition, analysis, and interpretation of the experimental data. This article has been authored by employees of National Technology & Engineering Solutions of Sandia, LLC, under Contract No. DE-NA0003525 with the USDOE. The employees co-own right, title, and interest in and to the article and are responsible for its contents. The United States Government retains and the publisher, by accepting the article for publication, acknowledges that the United States Government retains a nonexclusive, paid-up, irrevocable, worldwide license to publish or reproduce the published form of this article or allow others to do so, for United States Government purposes. The USDOE will provide public access to these results of federally sponsored research in accordance with the USDOE Public Access Plan https://www.energy.gov/downloads/doe-public-access-plan. A.J. was supported by the U.S. Department of Energy, Office of Science, Office of Basic Energy Sciences, Division of Chemical Sciences, Geosciences, and Biosciences under contract no. DE-AC02-06CH11357. J.A.F. acknowledges support from NSF through a CAREER Award (Grant CHE-2044927).

References

[1] C.W. Team, R.K. Pachauri, A. Reisinger, Climate Change 2007: Synthesis Report, in: P.R.K. Core Writing Team, A. Reisinger (Eds.), IPCC, Geneva, Switzerland, 2007, pp. 104.
[2] R. Saleh, From Measurements to Models: Toward Accurate Representation of Brown Carbon in Climate Calculations, Current Pollution Reports, 6 (2020).
[3] D.S. Jo, R.J. Park, S. Lee, S.W. Kim, X.L. Zhang, A global simulation of brown carbon: implications for photochemistry and direct radiative effect, Atmos. Chem. Phys., 16 (2016) 3413-3432.
[4] L. Zeng, A. Zhang, Y. Wang, N.L. Wagner, J.M. Katich, J.P. Schwarz, G.P. Schill, C. Brock, K.D. Froyd, D.M. Murphy, C.J. Williamson, A. Kupc, E. Scheuer, J. Dibb, R.J. Weber, Global Measurements of Brown Carbon and Estimated Direct Radiative Effects, Geophysical Research Letters, 47 (2020) e2020GL088747.
[5] R. Kusaka, S. Nihonyanagi, T. Tahara, The photochemical reaction of phenol becomes ultrafast at the air–water interface, Nature Chemistry, 13 (2021) 306-311.
[6] A. Laskin, J. Laskin, S.A. Nizkorodov, Chemistry of Atmospheric Brown Carbon, Chemical Reviews, 115 (2015) 4335-4382.
[7] E. Gómez Alvarez, H. Wortham, R. Strekowski, C. Zetzsch, S. Gligorovski, Atmospheric Photosensitized Heterogeneous and Multiphase Reactions: From Outdoors to Indoors, Environmental Science & Technology, 46 (2012) 1955-1963.
[8] S. Rossignol, K.Z. Aregahegn, L. Tinel, L. Fine, B. Nozière, C. George, Glyoxal Induced Atmospheric Photosensitized Chemistry Leading to Organic Aerosol Growth, Environmental Science & Technology, 48 (2014) 3218-3227.

[9] J.V. Trueblood, M.R. Alves, D. Power, M.V. Santander, R.E. Cochran, K.A. Prather, V.H. Grassian, Shedding Light on Photosensitized Reactions within Marine-Relevant Organic Thin Films, ACS Earth and Space Chemistry, 3 (2019) 1614-1623.
[10] A. Austin, G.A. Petersson, M.J. Frisch, F.J. Dobek, G. Scalmani, K. Throssell, A Density Functional with Spherical Atom Dispersion Terms, Journal of Chemical Theory and Computation, 8 (2012) 4989-5007.
[11] K.Z. Aregahegn, B. Nozière, C. George, Organic aerosol formation photo-enhanced by the formation of secondary photosensitizers in aerosols, Faraday Discussions, 165 (2013) 123-134.
[12] X. Wang, R. Gemayel, N. Hayeck, S. Perrier, N. Charbonnel, C. Xu, H. Chen, C. Zhu, L. Zhang, L. Wang, S.A. Nizkorodov, X. Wang, Z. Wang, T. Wang, A. Mellouki, M. Riva, J. Chen, C. George, Atmospheric Photosensitization: A New Pathway for Sulfate Formation, Environmental Science & Technology, 54 (2020) 3114-3120.
[13] H. Fu, R. Ciuraru, Y. Dupart, M. Passananti, L. Tinel, S. Rossignol, S. Perrier, D.J. Donaldson, J. Chen, C. George, Photosensitized Production of Atmospherically Reactive Organic Compounds at the Air/Aqueous Interface, Journal of the American Chemical Society, 137 (2015) 8348-8351.
[14] J. Lin, Q. Dai, H. Zhao, H. Cao, T. Wang, G. Wang, C. Chen, Photoinduced Release of Volatile Organic Compounds from Fatty Alcohols at the Air–Water Interface: The Role of Singlet Oxygen Photosensitized by a Carbonyl Group, Environmental Science & Technology, 55 (2021) 8683-8690.
[15] P.A. Alpert, R. Ciuraru, S. Rossignol, M. Passananti, L. Tinel, S. Perrier, Y. Dupart, S.S. Steimer, M. Ammann, D.J. Donaldson, C. George, Fatty Acid Surfactant Photochemistry Results in New Particle Formation, Scientific Reports, 7 (2017) 12693.
[16] M.E. Monge, T. Rosenørn, O. Favez, M. Müller, G. Adler, A. Abo Riziq, Y. Rudich, H. Herrmann, C. George, B. D'Anna, Alternative pathway for atmospheric particles growth, Proceedings of the National Academy of Sciences, 109 (2012) 6840-6844.
[17] S.L. Mora Garcia, S. Pandit, J.G. Navea, V.H. Grassian, Nitrous Acid (HONO) Formation from the Irradiation of Aqueous Nitrate Solutions in the Presence of Marine Chromophoric Dissolved Organic Matter: Comparison to Other Organic Photosensitizers, ACS Earth and Space Chemistry, 5 (2021) 3056-3064.
[18] L. Tinel, S. Rossignol, A. Bianco, M. Passananti, S. Perrier, X. Wang, M. Brigante, D.J. Donaldson, C. George, Mechanistic Insights on the Photosensitized Chemistry of a Fatty Acid at the Air/Water Interface, Environmental Science & Technology, 50 (2016) 11041-11048.
[19] P. Corral Arroyo, T. Bartels-Rausch, P.A. Alpert, S. Dumas, S. Perrier, C. George, M. Ammann, Particle-Phase Photosensitized Radical Production and Aerosol Aging, Environmental Science & Technology, 52 (2018) 7680-7688.
[20] T. Felber, T. Schaefer, L. He, H. Herrmann, Aromatic Carbonyl and Nitro Compounds as Photosensitizers and Their Photophysical Properties in the Tropospheric Aqueous Phase, J. Phys. Chem. A, 125 (2021) 5078-5095.
[21] N. Karimova, O. Alija, S.L.M. García, V.H. Grassian, R.B. Gerber, J.G. Navea, pH Dependence of the speciation and optical properties of 4-benzoylbenzoic acid, Phys. Chem. Chem. Phys., 25 (2023) 17306-17319.
[22] K.J. Angle, D.R. Crocker, R.M.C. Simpson, K.J. Mayer, L.A. Garofalo, A.N. Moore, S.L. Mora Garcia, V.W. Or, S. Srinivasan, M. Farhan, J.S. Sauer, C. Lee, M.A. Pothier, D.K. Farmer, T.R. Martz, T.H. Bertram, C.D. Cappa, K.A. Prather, V.H. Grassian, Acidity across the interface from the ocean surface to sea spray aerosol, Proc Natl Acad Sci U S A, 118 (2021) e2018397118.

[23] N.C. Frederiks, A. Hariharan, C.J. Johnson, Spectroscopic Studies of Clusters of Atmospheric Relevance, Annual Review of Physical Chemistry, 74 (2023) 99-121.
[24] S. Enami, L.A. Stewart, M.R. Hoffmann, A.J. Colussi, Superacid Chemistry on Mildly Acidic Water, The Journal of Physical Chemistry Letters, 1 (2010) 3488-3493.
[25] D. Konstantinovsky, T. Santiago, M. Tremblay, G.J. Simpson, S. Hammes-Schiffer, E.C.Y. Yan, Theoretical basis for interpreting heterodyne chirality-selective sum frequency generation spectra of water, The Journal of Chemical Physics, 160 (2024) 055102.
[26] A.P. Fellows, Á.D. Duque, V. Balos, L. Lehmann, R.R. Netz, M. Wolf, M. Thämer, Sum-Frequency Generation Spectroscopy of Aqueous Interfaces: The Role of Depth and Its Impact on Spectral Interpretation, The Journal of Physical Chemistry C, 128 (2024) 20733-20750.
[27] M.D. Baer, D.J. Tobias, C.J. Mundy, Investigation of Interfacial and Bulk Dissociation of HBr, HCl, and HNO3 Using Density Functional Theory-Based Molecular Dynamics Simulations, The Journal of Physical Chemistry C, 118 (2014) 29412-29420.
[28] S. Gopalakrishnan, D. Liu, H.C. Allen, M. Kuo, M.J. Shultz, Vibrational Spectroscopic Studies of Aqueous Interfaces: Salts, Acids, Bases, and Nanodrops, Chemical Reviews, 106 (2006) 1155-1175.
[29] H. Mishra, S. Enami, R.J. Nielsen, L.A. Stewart, M.R. Hoffmann, W.A. Goddard, A.J. Colussi, Brønsted basicity of the air–water interface, Proceedings of the National Academy of Sciences, 109 (2012) 18679-18683.
[30] P. Jungwirth, D.J. Tobias, Ions at the Air/Water Interface, The Journal of Physical Chemistry B, 106 (2002) 6361-6373.
[31] J. Zhong, M. Kumar, J.M. Anglada, M.T.C. Martins-Costa, M.F. Ruiz-Lopez, X.C. Zeng, J.S. Francisco, Atmospheric Spectroscopy and Photochemistry at Environmental Water Interfaces, Annual Review of Physical Chemistry, 70 (2019) 45-69.
[32] J.K. Denton, P.J. Kelleher, M.A. Johnson, M.D. Baer, S.M. Kathmann, C.J. Mundy, B.A. Wellen Rudd, H.C. Allen, T.H. Choi, K.D. Jordan, Molecular-level origin of the carboxylate head group response to divalent metal ion complexation at the air–water interface, Proceedings of the National Academy of Sciences, 116 (2019) 14874-14880.
[33] R.A. Relph, T.L. Guasco, B.M. Elliott, M.Z. Kamrath, A.B. McCoy, R.P. Steele, D.P. Schofield, K.D. Jordan, A.A. Viggiano, E.E. Ferguson, M.A. Johnson, How the Shape of an H-Bonded Network Controls Proton-Coupled Water Activation in HONO Formation, Science, 327 (2010) 308-312.
[34] E. Garand, Spectroscopy of Reactive Complexes and Solvated Clusters: A Bottom-Up Approach Using Cryogenic Ion Traps, The Journal of Physical Chemistry A, 122 (2018) 6479-6490.
[35] N. Heine, K.R. Asmis, Cryogenic ion trap vibrational spectroscopy of hydrogen-bonded clusters relevant to atmospheric chemistry, International Reviews in Physical Chemistry, 34 (2015) 1-34.
[36] A.B. Wolk, C.M. Leavitt, E. Garand, M.A. Johnson, Cryogenic Ion Chemistry and Spectroscopy, Accounts of Chemical Research, 47 (2014) 202-210.
[37] A. Cirri, H. Morales Hernández, C. Kmiotek, C.J. Johnson, Systematically Tuning the Electronic Structure of Gold Nanoclusters through Ligand Derivatization, Angewandte Chemie International Edition, 58 (2019) 13818-13822.
[38] L. Chen, J.L.S. Dean, J.A. Fournier, Time-Domain Vibrational Action Spectroscopy of Cryogenically Cooled, Messenger-Tagged Ions Using Ultrafast IR Pulses, The Journal of Physical Chemistry A, 125 (2021) 10235-10244.

[39] P. Pracht, F. Bohle, S. Grimme, Automated exploration of the low-energy chemical space with fast quantum chemical methods, Physical Chemistry Chemical Physics, 22 (2020) 7169-7192.
[40] A.D. Becke, Density-functional thermochemistry. III. The role of exact exchange, The Journal of Chemical Physics, 98 (1993) 5648-5652.
[41] C. Lee, W. Yang, R.G. Parr, Development of the Colle-Salvetti correlation-energy formula into a functional of the electron density, Physical Review B, 37 (1988) 785-789.
[42] S.H. Vosko, L. Wilk, M. Nusair, Accurate spin-dependent electron liquid correlation energies for local spin density calculations: a critical analysis, Canadian Journal of Physics, 58 (1980) 1200-1211.
[43] P.J. Stephens, F.J. Devlin, C.F. Chabalowski, M.J. Frisch, Ab Initio Calculation of Vibrational Absorption and Circular Dichroism Spectra Using Density Functional Force Fields, The Journal of Physical Chemistry, 98 (1994) 11623-11627.
[44] W.J. Hehre, R.F. Stewart, J.A. Pople, Self-Consistent Molecular-Orbital Methods. I. Use of Gaussian Expansions of Slater-Type Atomic Orbitals, The Journal of Chemical Physics, 51 (1969) 2657-2664.
[45] S. Grimme, S. Ehrlich, L. Goerigk, Effect of the damping function in dispersion corrected density functional theory, Journal of Computational Chemistry, 32 (2011) 1456-1465.
[46] R.A. Kendall, T.H. Dunning, Jr., R.J. Harrison, Electron affinities of the first-row atoms revisited. Systematic basis sets and wave functions, The Journal of Chemical Physics, 96 (1992) 6796-6806.
[47] D.E. Woon, T.H. Dunning, Jr., Gaussian basis sets for use in correlated molecular calculations. III. The atoms aluminum through argon, The Journal of Chemical Physics, 98 (1993) 1358-1371.
[48] A.T.B. Gilbert, IQmol molecular viewer.
[49] N. Yang, C.H. Duong, P.J. Kelleher, A.B. McCoy, M.A. Johnson, Deconstructing water's diffuse OH stretching vibrational spectrum with cold clusters, Science, 364 (2019) 275-278.
[50] L. Chen, E.L. Sibert, III, J.A. Fournier, Unraveling the Vibrational Spectral Signatures of a Dislocated H Atom in Model Proton-Coupled Electron Transfer Dyad Systems, The Journal of Physical Chemistry A, 127 (2023) 3362-3371.
[51] W.H. Robertson, E.G. Diken, E.A. Price, J.-W. Shin, M.A. Johnson, Spectroscopic Determination of the OH− Solvation Shell in the OH−·(H2O)n Clusters, Science, 299 (2003) 1367-1372.
[52] P. Ayotte, C.G. Bailey, G.H. Weddle, M.A. Johnson, Vibrational Spectroscopy of Small Br-·(H2O)n and I-·(H2O)n Clusters: Infrared Characterization of the Ionic Hydrogen Bond, The Journal of Physical Chemistry A, 102 (1998) 3067-3071.
[53] W.H. Robertson, E.A. Price, J.M. Weber, J.-W. Shin, G.H. Weddle, M.A. Johnson, Infrared Signatures of a Water Molecule Attached to Triatomic Domains of Molecular Anions: Evolution of the H-bonding Configuration with Domain Length, The Journal of Physical Chemistry A, 107 (2003) 6527-6532.
[54] N.C. Frederiks, C.J. Johnson, Photochemical Mechanisms in Atmospherically Relevant Iodine Oxide Clusters, The Journal of Physical Chemistry Letters, 15 (2024) 6306-6314.
[55] V. Vaida, Sunlight initiated atmospheric photochemical reactions, International Journal of Photoenergy, 7 (2005) 825218.